ACS Catalysis

Research Article

pubs.acs.org/acscatalysis

Kinetic Regime Change in the Tandem Dehydrative Aromatization of Furan Diels–Alder Products

Ryan E. Patet,[†,∥,⊥] Nima Nikbin,[†,∥,⊥] C. Luke Williams,[§,∥,⊥] Sara K. Green,[§,∥] Chun-Chih Chang,[§,∥] Wei Fan,[§,∥] Stavros Caratzoulas,*[,†,∥] Paul J. Dauenhauer,*[,‡,∥] and Dionisios G. Vlachos*[,†,∥]

[†]Department of Chemical and Biomolecular Engineering, University of Delaware, Newark, Delaware 19716, United States

[‡]Department of Chemical Engineering and Materials Science, University of Minnesota, Minneapolis, Minnesota 55455, United States

[§]Department of Chemical Engineering, University of Massachusetts, Amherst, Massachusetts 01003, United States

[∥]Catalysis Center for Energy Innovation (CCEI), University of Delaware, Newark, Delaware 19716, United States, www.efrc.udel.edu

Supporting Information

ABSTRACT: Renewable production of *p*-xylene from [4 + 2] Diels–Alder cycloaddition of 2,5-dimethylfuran (DMF) and ethylene with H–Y zeolite catalyst in *n*-heptane solvent is investigated. Experimental studies varying the solid acid catalyst concentration reveal two kinetic regimes for the *p*-xylene production rate: (i) a linear regime at low acid site concentrations with activation energy E_a = 10.8 kcal/mol and (ii) a catalyst-independent kinetic regime at high acid site concentrations with activation energy E_a = 20.1 kcal/mol. We carry out hybrid QM/MM calculations with a three-layer embedded cluster ONIOM model to compute the energetics along the main reaction pathway, and a microkinetic model is constructed for the interpretation of the experimental kinetic data. At high solid acid concentrations, *p*-xylene production is limited by the homogeneous Diels–Alder reaction, whereas at low acid concentrations, the overall rate is limited by the heterogeneously catalyzed dehydration of the Diels–Alder cycloadduct of DMF and ethylene because of an insufficient number of acid sites, despite the dehydration reaction requiring significantly less activation energy. A reduced kinetic model reveals that the production of *p*-xylene follows the general kinetics of tandem reactions in which the first step is uncatalyzed and the second step is heterogeneously catalyzed. Reaction orders and apparent activation energies of quantum mechanical and microkinetic simulations are in agreement with experimental values.

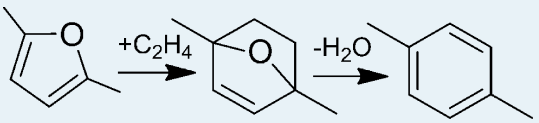

KEYWORDS: *p-xylene, 2,5-dimethylfuran (DMF), ethylene, Diels–Alder, dehydration, faujasite, microkinetic model*

1.0. INTRODUCTION

Research into the production of biorenewable fuels and chemicals has rapidly expanded in the past decade in an effort to reduce dependence on traditional, nonrenewable resources.[1,2] Coinciding with the increased research effort into biomass-derived fuels and chemicals, shale gas production has also greatly expanded in the United States. This newly tapped energy source has the potential to provide vast quantities of C_1 and C_2 hydrocarbons but lacks the ability to provide larger olefins and aromatic chemicals.[3] Within this framework, utilization of biomass-derived sugars has the potential to provide the chemical industry with a more feedstock-diverse source of C_4+ and aromatic chemicals that is close to carbon-neutral.[4−8]

One major biorenewable chemical of interest is *p*-xylene, which may be produced from biomass-derived 2,5-dimethylfuran (DMF) and ethylene. DMF can be produced from glucose via hydroxymethylfurfural,[9,10] and ethylene can be obtained from dehydration of biomass-derived ethanol.[11,12] Diels–Alder [4 + 2] cycloaddition of DMF and ethylene has been shown to form an oxanorbornene cycloadduct in a single elementary step, after which multistep dehydration forms *p*-xylene and water.[13,14] Renewable *p*-xylene has been proposed as a source for the production of terephthalic acid, which is used in the manufacture of plastic bottles, clothing, automobile components, and many other products.[15,16] Efforts to maximize the production of *p*-xylene from DMF have demonstrated 90% *p*-xylene yield over H-BEA zeolite in heptane solvent.[17] Heptane has proven effective at greatly reducing competing side reactions, such as alkylation of *p*-xylene with ethylene, formation of polymers from aromatics and furans, and hydrolysis of the furan by the water produced in the dehydrative aromatization (Figure 1).[13,18]

Despite a high yield of *p*-xylene formation from dimethylfuran, the role of the active catalytic site of H–Y zeolites and associated kinetics remains to be understood. The rate at which *p*-xylene is produced with a H–Y (Si/Al 2.6–40) zeolite catalyst has been reported to be independent of the number of available Brønsted acid sites,[19] and thus, it was inferred that the rate-limiting step should be *uncatalyzed*. However, in a different study of the reaction of DMF and ethylene with WO_x–ZrO_2 catalyst, the rate of formation of *p*-xylene was instead reported as having linear dependence on the density of acid sites.[20] Quantum chemical calculations have shown that Brønsted acids

Received: December 23, 2014
Revised: February 19, 2015

DOI: 10.1021/cs5020783
ACS Catal. 2015, 5, 2367−2375

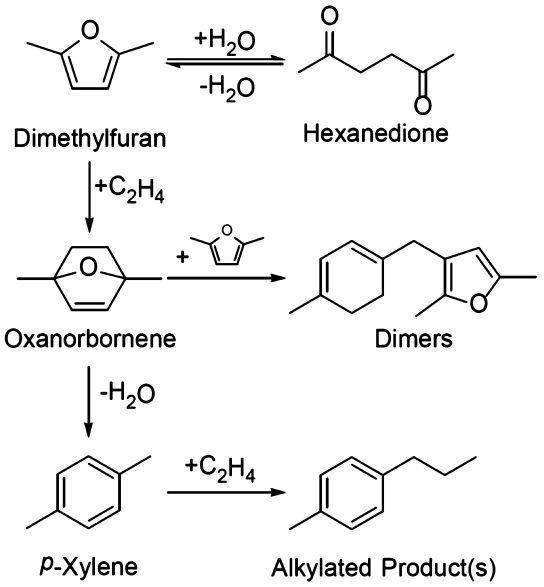

Figure 1. Reactions in the production of *p*-Xylene from DMF and ethylene.

do not significantly catalyze the Diels–Alder reaction between furans and ethylene.[13,14,21] Acidic protons have a higher affinity for the furan than ethylene and, in particular, for the ring carbons of the furan—where the HOMO amplitude is the largest—which breaks the requisite orbital symmetry for [4 + 2] cycloaddition.[13,14,22] However, the second reaction, dehydration of the Diels–Alder cycloadduct of DMF and ethylene, cannot proceed uncatalyzed; Brønsted acids reduce the kinetic energy barrier by as much as 45 kcal/mol and are essential for this step.[13,14,21]

Variation in the dependence of the rate of *p*-xylene formation on the type and concentration of Brønsted acids thus raises intriguing questions about the kinetics of the reaction (cycloadduct formation and subsequent dehydration to *p*-xylene, as shown in Figure 1) and more generally about the kinetics of tandem reactions, which, in conjunction with bifunctional catalysts can be utilized in the design of efficient, one-pot synthetic processes. In this article, we present kinetic data that show that the concentration of Brønsted acid sites gives rise to two distinct kinetic regimes in the tandem scheme of Diels–Alder cycloaddition and dehydrative aromatization to *p*-xylene. Using hybrid quantum mechanics/molecular mechanics (QM/MM) calculations and microkinetic modeling, we show that in the first kinetic regime, in which the overall rate of *p*-xylene formation grows linearly with the density of acid sites, the kinetics are controlled by the *catalyzed* dehydration of the Diels–Alder cycloadduct. In contrast, in the second regime, in which the rate is independent of the density of acid sites, the kinetic bottleneck is the *uncatalyzed* Diels–Alder reaction. At high catalyst loadings, there are enough free active sites to catalyze dehydration, and as a result, the homogeneous Diels–Alder reaction becomes rate-limiting, consistent with the fact that this is the most energetically demanding step of the mechanism. The linear regime occurs at low catalyst loadings, and because there are not enough active sites to catalyze it, the dehydrative aromatization reaction becomes rate-controlling, despite the fact that it requires a lower activation energy than the cycloaddition reaction. Finally, we present a reduced kinetic model to show that the two regimes are characteristic of tandem schemes in which the first reaction proceeds uncatalyzed while the second reaction does so catalyzed.

2.0. METHODS

2.1. Experiment. Experiments examined the kinetics of the reaction of DMF and ethylene with faujasite catalysts within gas/liquid/solid reactors.

2.1.1. Reaction Setup. Reactions were performed in Parr 4560 series reactors equipped with 4848 controllers and gas entrainment impellers to eliminate mass transport limitations. Chemicals were used without further purification and consisted of 2,5-dimethylfuran (Alfa Aesar 98+%), *n*-heptane (Alfa Aesar

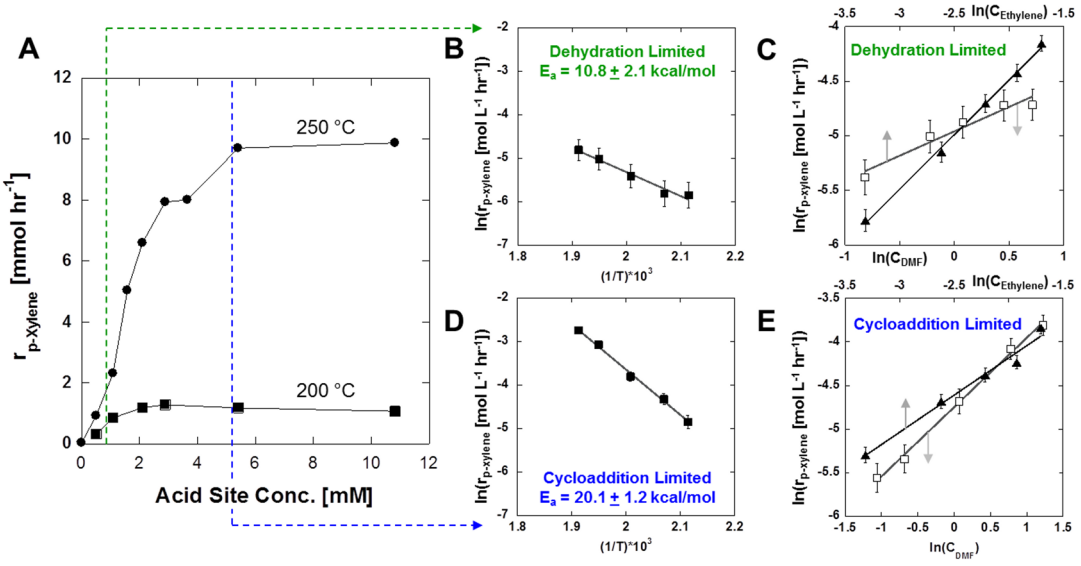

Figure 2. Kinetics of *p*-xylene production with H–Y zeolite catalyst: experiment. (A) Rate of *p*-xylene production at 200 and 250 °C relative to strong acid site concentration. (B) Arrhenius plot at 1.3 mM H–Y acid site concentration. (C) *p*-Xylene reaction rate with respect to dimethylfuran (DMF; □) and ethylene (▲) at 1.3 mM H–Y acid site concentration. (D) Arrhenius plot at 1.3 mM H–Y acid site concentration. (E) *p*-Xylene reaction rate with respect to dimethylfuran (DMF; □) and ethylene (▲) at 5.1 mM H–Y acid site concentration.

DOI: 10.1021/cs5020783
ACS Catal. 2015, 5, 2367–2375

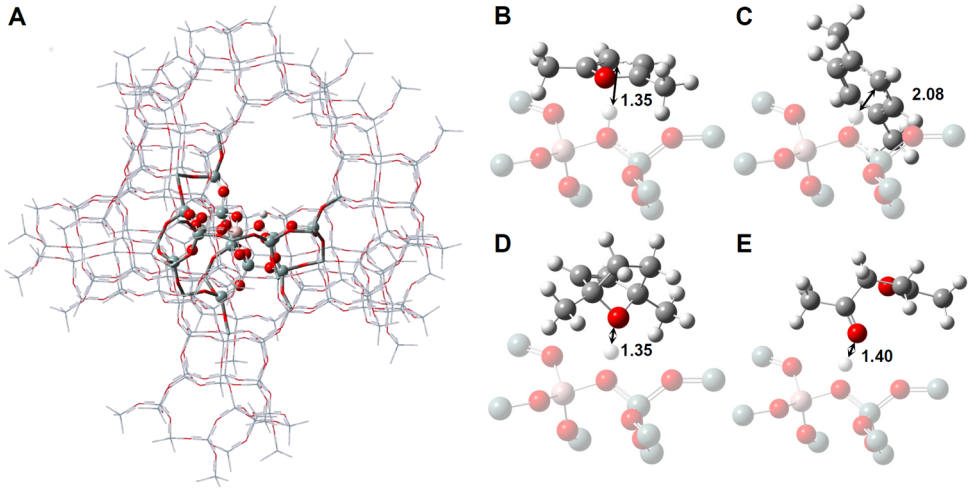

Figure 3. Adsorption of dimethylfuran, *p*-xylene, oxanorbornene and hexanedione in faujasite. (A) ONIOM model (218T) used for adsorption calculations where atoms represented by balls-and-sticks are in the high layer, tube frames are in the intermediate layer, and wireframes are in the low layer (white, hydrogen; gray, carbon; red, oxygen; pink, aluminum; and green-gray, silicon). Adsorption complexes extracted from the ONIOM model of (B) DMF, (C) *p*-xylene, (D) oxanorbornene, and (E) 2,5-hexanedione are also shown, where the distances from the active site proton to the nearest atom of the adsorbate are provided in units of Å.

99+%), ethylene gas (Airgas UHP), and *n*-tridecane (Sigma-Aldrich 98+%) as an internal standard. An H−Y faujasite catalyst with a Si/Al ratio of 2.6 (Zeolyst CBV 600) was used for all of the reactions and dried in a furnace at 200 °C prior to use. Reaction procedure involved loading the vessel with DMF, heptane, tridecane, and catalyst prior to heating and initiation of the reaction by adding 200 psi of ethylene gas and maintaining pressure throughout the course of the experiment. Additionally, the second Damköhler number was estimated to be equal to 0.0002 ≪ 0.1, which indicates the absence of mass transfer limitations between gaseous and solution phase ethylene (Figure S1). The reaction rate was found to be independent of particle size, which implies that intraparticle diffusion is not rate limiting either.

2.1.2. Reaction Orders and Activation Energies. Dependence of reaction rate on catalyst loading was investigated using 1.38 M DMF in *n*-heptane, with 0.082 M *n*-tridecane as an internal standard and 14 bar (200 psi) ethylene pressure. These initial concentrations and pressures were used as the standard reaction conditions. Experiments investigating the reaction regimes of Figure 2 were performed at 200 and 250 °C by varying the catalyst loading from 0.3 to 1.5 g to yield effective Brønsted acid site concentrations between 1.1 and 5.1 mM. Experiments investigating the parameters of reaction rate expressions (i.e., reaction orders) were performed at low and high catalyst loadings (1.3 and 5.1 mM) for both DMF and ethylene at 200 °C. The concentration of DMF in DMF reaction order experiments varied from 0.46 to 2.3 M in 0.46 M increments. In ethylene reaction order experiments, the ethylene pressure varied from 6.9 to 34.5 bar in 6.9 bar increments (100−500 psi in 100 psi increments), yielding ethylene concentrations of 0.036−0.18 M in 0.036 M increments. Ethylene concentrations were estimated from previous measurements.[23] Experiments investigating the activation energies of Figure 2 were performed at 0.3 and 1.5 g by varying the temperature from 200 to 250 °C in 10 °C increments using the standard reaction conditions above.

2.1.3. Reaction-Product Characterization. Characterization of chemical components within the reaction mixture was performed with an Agilent 6890 gas chromatograph equipped with a G1513A autosampler, HP-Innowax column (to achieve separation of *o*,*m*,*p*-xylene isomers), and a flame ionization detector. Samples were collected under reaction conditions at high temperature and pressure utilizing a double block sampling system, which allows for samples to be taken without opening the reaction vessel. Major species were identified by matching retention times with pure standards. All reported data exhibited carbon balance closure greater than or equal to 90%.

2.2. Computational. Quantum mechanics/molecular mechanics (QM/MM) calculations have been used to calculate the relevant adsorption energies and reaction barriers for the chemistry of interest, using a three-layer, mechanically embedded ONIOM cluster model. The computed energies were then used to parametrize a microkinetic model.

2.2.1. QM/MM Calculations. The reaction pathway calculations were performed on a $HAlSi_{313}O_{520}$ cluster model (314 tetrahedral atoms) of H−Y. The model was cut out from the periodic structure of pure faujasite zeolite,[26] and the dangling bonds were saturated with hydrogen atoms. Three-layer ONIOM models[27−29] were employed to perform all calculations within the zeolite for the purposes of capturing the local active site and surrounding zeolite pore environments. For reactions within the zeolite, the high layer, comprising the active site and its environment (the active hexagonal ring and the six surrounding 4-T rings, a total of 18 T atoms, $HAlSi_{17}O_{24}$), was treated quantum mechanically with the M062X functional.[25] The adsorbates, the Brønsted H atom, the aluminum atom of the zeolite and the oxygen atoms in its first coordination shell, viz. nearest neighbors, were modeled with the 6-31G(d,p) basis set, while the rest of the high layer zeolite atoms were modeled with the effective core potential basis set LANL2DZ. The medium layer, the supercage in which the reaction takes place, was modeled at the M062*X*/3-21G level and kept frozen after optimization of the bare zeolite. For the modeling of the low ONIOM layer, the rest of the zeolite cluster, we employed the molecular mechanics force field UFF;[30] the atoms of this layer were kept frozen in their crystallographic positions at all times. The zeolite was optimized in the absence of adsorbates and only the high layer was allowed to relax in the presence of adsorbates.

DOI: 10.1021/cs5020783
ACS Catal. 2015, 5, 2367−2375

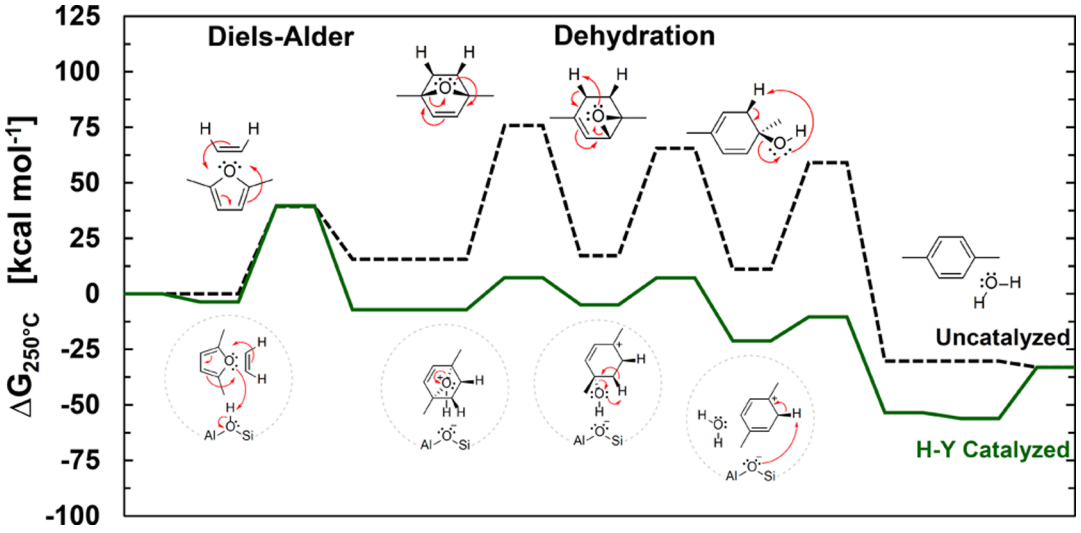

Figure 4. Free energy profile of *p*-xylene production from DMF and ethylene. Diels–Alder cycloaddition of DMF and ethylene followed by dehydrative aromatization occurs in the absence (dashed line; homogeneous phase) and presence (solid line; heterogeneous phase) of H–Y zeolite. Calculated intermediate and transition states account for the influence of the zeolite pore.

Binding energies are sensitive to the basis set of the quantum mechanical region and susceptible to basis set superposition error. Thus, for the adsorption of reactants, intermediates, and products within the zeolite H–Y, we used a second ONIOM model with a slightly smaller high layer which, however, allowed us to use triple-ζ valence basis functions and additional polarization. In this model consisting of 218 tetrahedral atoms ($HAlSi_{217}O_{352}$), the high layer consisted of the 14 T atoms in the first two coordination spheres around the substituted aluminum atom and was modeled at the M062*X*/6-311G-(2df,p) level. The intermediate layer included the 16 T atoms in the third coordination sphere around the substituted aluminum atom and was modeled at the M062*X*/3-21G level and kept frozen. The remaining 188 T atoms in the fourth through sixth coordination spheres were modeled with the molecular mechanics force field UFF, with atoms being kept frozen in their crystallographic positions. This model was benchmarked against adsorption experimental data (not shown). Solution phase calculations of isolated reactants and products were performed with the SMD model[24] at the M062*X*/6-311G(2df,p) theory level. All calculations were performed with the Gaussian 09 (Rev. A.2) program.[31]

2.2.2. Reaction Network. The reaction network consists of the following reactions: homogeneous and heterogeneous Diels–Alder cycloaddition of DMF and ethylene; homogeneous and heterogeneous cycloadduct dehydration comprising of three elementary reaction steps (Figure 3); heterogeneous DMF hydrolysis;[13,32] and adsorption/desorption steps of reactants, products and stable intermediates.[13,14]

2.2.3. Reaction Rate Constants and Microkinetic Modeling. The calculated free energies of activation and reaction were used to parametrize a microkinetic model, as detailed in the Supporting Information. Given the uncertainty in QM/MM calculations and especially in the entropic contributions to the free energies of reaction and activation, we introduced a design of experiment (DOE) approach to investigate the sensitivity of multiple, experimentally measured parameters (*p*-xylene production rate, apparent activation energy, and reaction orders) to multiple model parameters (the binding strength of oxanorbornene, DMF, and hexanedione to the active site, the homogeneous Diels–Alder Gibbs free energy of reaction, and the heterogeneous dehydration reaction barrier), which were identified to be important through sensitivity analysis of the microkinetic model. This methodological innovation departs from the traditional single-parameter-change-at-a-time sensitivity analysis and is reminiscent of global sensitivity analysis subject to constraints imposed by our experimental measurements. Details of this approach can be found in the Supporting Information, and the final set of parameters used to build the microkinetic model can be found in Table S1. All adjustments to the final parameters were found to be within the expected computational error. A global sensitivity analysis was also performed.

3.0. RESULTS AND DISCUSSION

3.1. Experimental Kinetics of Reaction of DMF and Ethylene. The rate of *p*-xylene production exhibits complex dependence on the relative concentrations of reactants (DMF and ethylene) and strong acid sites in H–Y zeolite. As shown in Figure 2A, the rate of *p*-xylene production at 200 and 250 °C exhibits linear dependence on the concentration of strong Brønsted acid sites at the given conditions and low acid site concentrations (<3.0 mM). However, above ~3.0 mM acid site concentration, the rate of *p*-xylene formation becomes independent of strong acid site concentration; for these conditions, the addition of more catalyst has no impact on the overall formation rate of *p*-xylene ($r_{p\text{-xylene}} \propto [H^+]^Z$, $Z \sim 0$).

Differences in the two regimes of Figure 2 extend to the measurable kinetic parameters. As depicted in Figure 2B,D, Arrhenius plots generated at low acid site concentration (1.3 mM $[H^+]$) and high acid site concentration (5.1 mM $[H^+]$) exhibit statistically different activation energies: low acid concentration conditions lead to an activation energy of 10.8 ± 2.1 kcal/mol, and high acid concentration conditions exhibit an activation energy of 20.1 ± 1.2 kcal/mol. Moreover, the rate of formation of *p*-xylene exhibits variable dependence on the reactant concentrations between the two kinetic regimes, as measured at 200 °C. At low acid concentration (1.3 mM $[H^+]$), the reaction rate expression for *p*-xylene formation has first-order dependence on ethylene ($r_{p\text{-xylene}} \propto [C_2H_4]^X$, X = 1.01 ±

DOI: 10.1021/cs5020783
ACS Catal. 2015, 5, 2367–2375

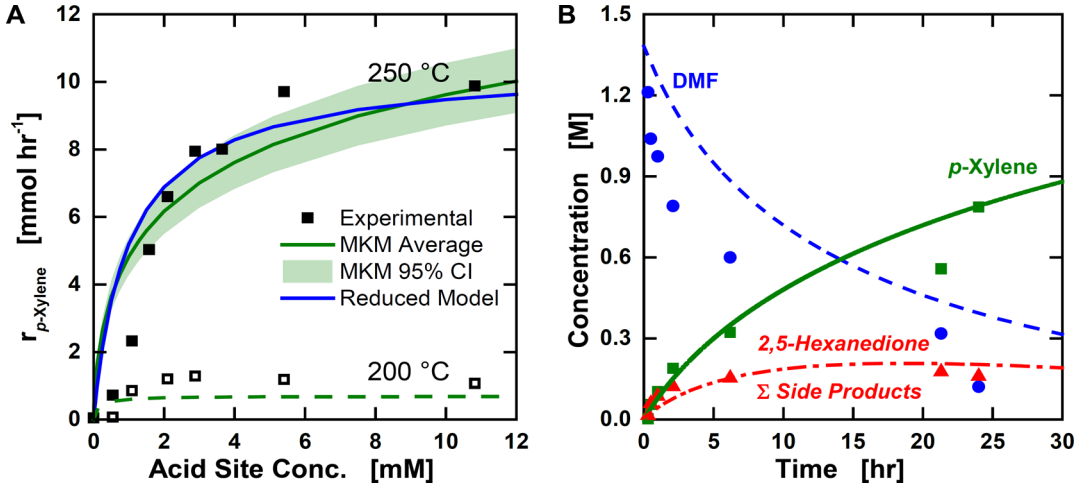

Figure 5. Model comparisons with experimentally available data. (A) *p*-Xylene initial production rate at Bronsted acid concentrations at 250 °C. *p*-Xylene production rates are calculated as the average rate over the first 50 min of reaction time at the specified temperature and catalyst loading. (B) Solution-phase composition experiments (points) and simulations (lines). Conditions: 2.0 g of H−Y (Si/Al = 2.6) for an effective acid site concentration of 6.8 mM, 1.38 M DMF, at 250 °C. MKM results are shown as lines, and experimental data are shown as points. The values in red are the solution phase concentration of 2,5-hexanedione from the model and the sum of all side products from the experimental data.

0.07) and half-order dependence on dimethylfuran ($r_{p\text{-xylene}} \propto [\text{DMF}]^{Y}$, $Y = 0.49 \pm 0.08$), determined from the data of Figure 2. However, at high acid concentrations (5.1 mM [H^+]), the rate of *p*-xylene formation exhibits closer to first-order dependence in both ethylene and DMF ($r_{p\text{-xylene}} \propto [C_2H_4]^{X}[\text{DMF}]^{Y}$; $X = 0.90 \pm 0.13$, $Y = 0.79 \pm 0.07$), as determined from the data of Figure 2E.

3.2. QM/MM Calculations of Relevant Energies and Barriers. Calculation of the adsorption of reactants, intermediates, products, and transition states within the zeolite pore environment provides mechanistic understanding of the chemistry at the strong acid site within H−Y. The calculated adsorption strengths from the $HAlSi_{217}O_{352}$ ONIOM model can be found in Table S1 and Figure 3. Calculations show that among the reactants and products, DMF (17.9 kcal/mol) and *p*-xylene (16.6 kcal/mol) bind more strongly to the active site than either ethylene (9.0 kcal/mol) or water (11.1 kcal/mol). Examining the DMF and *p*-xylene adsorption geometries on the catalyst surface (Figure 3B and 3C), we see that both molecules coordinate to the active site with their aromatic carbons atoms. The oxanorbornene intermediate formed by the Diels−Alder cycloaddition reaction of DMF and ethylene strongly adsorbs to the surface of the zeolite (25.8 kcal/mol), with the bridging oxygen atom located closest to the active site (Figure 3D). 2,5-Hexanedione, formed by the hydrolysis of DMF with water, also binds strongly (25.9 kcal/mol), with an oxygen from one of the keto groups being closest to the active site (Figure 3E).

Tandem Diels−Alder reaction and subsequent dehydrative aromatization pathways within Brønsted acidic zeolites have been previously discussed;[13,14,21] here, we provide comprehensive energetics of all elementary steps, obtained from ONIOM calculations on the $HAlSi_{313}O_{520}$ cluster model (Figure 4), and detailed understanding of the dominant reaction pathways via a microkinetic model (MKM). Energies for the uncatalyzed reaction mechanism in Figure 4 show that the Diels−Alder reaction has a barrier of 39.5 kcal/mol, and the largest barrier of the subsequent dehydration of the oxanorbornene intermediate is 60.1 kcal/mol. In the calculations from the ONIOM model accounting for catalysis at the H−Y zeolite active site and surrounding pore, the Diels−Alder reaction barrier of dimethylfuran and ethylene remains about the same, with a barrier of 43.4 kcal/mol; however, there is a significant decrease in the largest dehydration reaction barrier to 14.4 kcal/mol. From the depicted reaction barriers of Figure 4, it is clear that H−Y does not catalyze the Diels−Alder reaction between DMF and ethylene. Dehydration of the oxanorbornene cycloadduct is, however, orders of magnitude faster in the Brønsted acidic zeolite H−Y. Fast proton transfer from the zeolite active site to the bridging oxygen atom initiates the reaction. The oxanorbornene oxygen bridge, C2−O, breaks with activation energy of only 14.4 kcal/mol, which is 45.7 kcal/mol lower than the uncatalyzed reaction barrier. The binding of the proton to the bridging oxygen appears to stabilize the transition state for the C2−O cleavage, making this reaction much more favorable. In the acid catalyzed case, the slowest step along this pathway is the uncatalyzed Diels−Alder cycloaddition. The furan ring of DMF may open hydrolytically upon *β*-C protonation and subsequent water addition at the adjacent *α*-C.[32]

3.3. Microkinetic Model Results and Discussion. By the calculated energies of Figure 4, one would conclude that Diels−Alder cycloaddition should be the rate-limiting reaction for all acid-catalyzed reactions, a result differing from the experimental results of Figure 2, which indicates two distinct kinetic regimes. To probe the kinetics of the acid-catalyzed system, the QM/MM calculations for adsorption energies and reaction barriers were used to develop a microkinetic model (MKM) by the details provided in the Methods section and Table S1.

Figure 5A shows the predicted rate of *p*-xylene production as a function of acid site concentration from the MKM. The MKM (green line) agrees well with experimental data at 200 and 250 °C. The two kinetic regimes were captured by the MKM: at low acid site concentrations, the *p*-xylene production rate varies with the acid site concentration, whereas at high acid site concentrations, the *p*-xylene production rate is independent of acid site concentration. In addition, a global sensitivity analysis was performed on the MKM model such that the adsorption strength of oxanorbornene and DMF to the active site, the homogeneous Diels−Alder Gibbs free energy of reaction, and the heterogeneous dehydration reaction barrier

DOI: 10.1021/cs5020783
ACS Catal. 2015, 5, 2367−2375

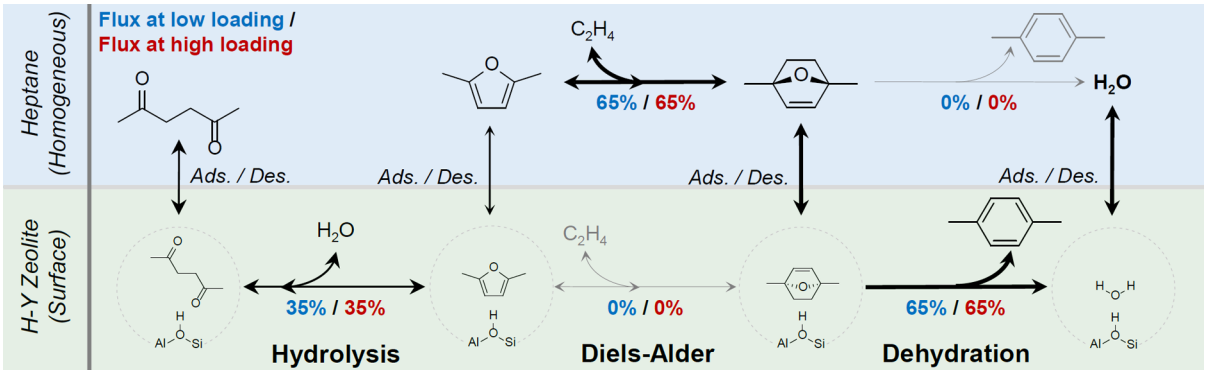

Figure 6. Abridged reaction network and simulation reaction path fluxes. Diels–Alder and dehydration reactions in homogeneous (green) and heterogeneous (blue) phases and hydrolysis of DMF. Inactive pathways are represented in gray. Fluxes calculated by the MKM model are provided as percentages of the total flux of DMF initially fed into the reactor averaged over the first 50 min of reaction at 250 °C at Brønsted acid site concentrations of 0.1 mM (low loading, blue) and 5.1 mM (high loading, red).

provided a confidence interval that indicated that the parametrized model was robust in describing the *p*-xylene production rate. These energies were independently perturbed using a normal distribution with a standard deviation of 1.5 kcal/mol. The 95% confidence interval, depicted as a green region in Figure 5A, encompassed the data points of *p*-xylene production rate at 250 °C.

Figure 5B depicts the solution phase concentrations predicted by the MKM with reaction time. Consumption of DMF and formation of *p*-xylene predicted by the model are in agreement with experiments. A consumption rate of DMF slower than expected could be because the model does not include side reactions other than DMF hydrolysis to hexanedione. Further Diels–Alder reaction between DMF and the cycloadduct or unproductive pathways through the dehydrative aromatization intermediates can also be responsible for loss of DMF, but they are not considered in the current model.[18] Nevertheless, the close agreement between the experimental and model concentration profiles that 2,5-hexanedione makes up the majority of side products present in the reaction. The 2,5-hexanedione that is formed is able to reversibly convert back into DMF to be further converted into *p*-xylene, and therefore, as the conversion of DMF increases, the thermodynamics of the system reduce the presence of 2,5-hexanedione product found in solution and help drive the system to high yields of *p*-xylene.

Analysis of the MKM (Figure 6) provides detailed understanding of the active reaction pathways. For both the high (5.1 mM [H^+], red) and low (0.1 mM [H^+], blue) catalyst loading scenarios, the reaction pathway to *p*-xylene is the same. The homogeneous Diels–Alder reaction accounts for 65% of the flux of DMF in solution in a reversible reaction, and the remaining DMF in solution adsorbs on the catalyst surface and undergoes hydrolysis with water to 2,5-hexanedione. It can be seen that the adsorbed DMF does not undergo heterogeneous Diels–Alder reaction, but rather, a hydrolysis reaction. Of the oxanorbornene formed by homogeneous Diels–Alder reaction, it can be seen that none of it is homogeneously dehydrated into *p*-xylene and water, as a result of the prohibitively high reaction barrier. Rather, all of the oxanorbornene adsorbs on the catalyst surface and undergoes irreversible, heterogeneous dehydration.

With the reaction path analysis revealing the major route for the reaction, uncatalyzed Diels–Alder reaction followed by Brønsted acid catalyzed dehydration, we can examine differences between the two kinetic regimes. Rate-limiting steps for both kinetic regimes have been verified by performing sensitivity analysis of the MKM shown in Figure 7. At low

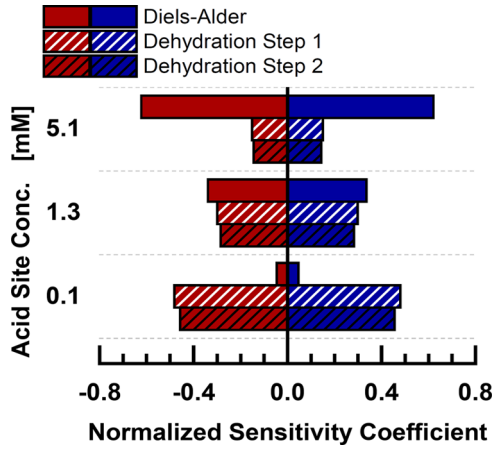

Figure 7. Sensitivity analysis of microkinetic model. The normalized sensitivity coefficient is defined as $\ln(r_{pX,Perturbed} - r_{pX,Unperturbed})/\ln(k_{i,Perturbed} - k_{i,Unperturbed})$. Reaction rate parameters were perturbed by +1% (blue) and −1% (red) at 250 °C for each of the catalyst loadings shown. Dehydration step 1 represents the C–O bond cleavage and dehydration step 2 represents the first proton transfer from the three-step mechanism seen in Figure 4.

acid site concentrations (0.1 mM [H^+]), the normalized sensitivity coefficients for the heterogeneous dehydration reaction steps (~0.45) are much greater than that of the homogeneous Diels–Alder reaction (0.05), indicating that the heterogeneous dehydration reaction is rate-limiting. In contrast, at high acid site concentrations (5.1 mM [H^+]), there is a clear shift in the normalized sensitivity coefficients (0.62 for the homogeneous Diels–Alder reaction compared with ~0.15 for the heterogeneous dehydration reaction), indicating that the homogeneous Diels–Alder reaction is rate-limiting.

Using the MKM, we have determined apparent activation energies and rate orders in the two kinetic regimes, namely, at 0.1, 1.3, and 5.1 mM [H^+], as shown in Table 1 and Figure 8A. We should note that although the 1.3 mM active site concentration clearly falls within the experimental linear regime (Figure 5A), the same cannot be said of the model. Thus, in the case of the MKM, we have also considered a catalyst loading of 0.1 mM to ensure that we were looking at values well within the model's linear regime and not in a transitional state between

DOI: 10.1021/cs5020783
ACS Catal. 2015, 5, 2367–2375

Table 1. Kinetic Parameters for Cycloaddition of Dimethylfuran and Ethylene at Different Brønsted Acid Site Concentrations[a]

	experiments		simulation		
kinetic parameter	low catalyst loading (1.3 mm)	high catalyst loading (5.1 mm)	low catalyst loading (0.1 mm)	low catalyst loading (1.3 mm)	high catalyst loading (5.1 mm)
DMF reaction order	0.49 ± 0.08	0.79 ± 0.07	0.30 ± 0.02	0.59 ± 0.03	0.73 ± 0.02
ethylene reaction order	1.01 ± 0.07	0.90 ± 0.13	0.99 ± 0.00	0.98 ± 0.00	0.98 ± 0.00
apparent activation energy (kcal/mol)	10.8 ± 2.1	20.1 ± 1.2	18.4 ± 0.2	21.3 ± 0.3	22.7 ± 0.3

[a]Error bars in simulations are the result of uncertainty quantification.

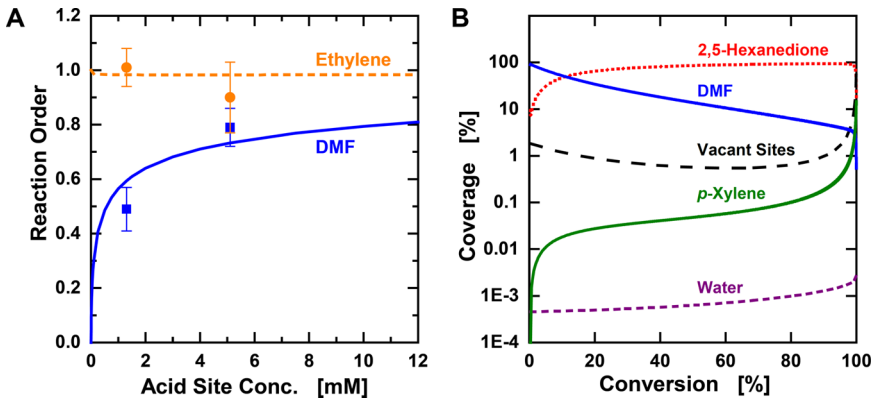

Figure 8. Microkinetic model output. (A) Reaction rate orders as a function of acid site concentration. MKM derived parameters are shown as lines, whereas experimental data is shown as points. (B) Surface coverage of H−Y active sites. Surface coverage of strong acid sites vary as a function of conversion at 250 °C at 5.1 mM of acid site concentration. Coverages do not change significantly when moving from low to high catalyst loading regimes. Oxanorbornene coverage (not shown) is less than 10^{-7}% at all conversions.

Table 2. Simulated Reactions and Kinetic Parameters

No.[a]	Reaction[b]	k_i[c]	$\Delta G^{\ddagger}_{250\ °C,i}$[d]	k_{-i}	$\Delta G^{\ddagger}_{250\ °C,-i}$[d]
1	**DMF + E ⇌ CA**	**3.5×10^{-4} M^{-1} s^{-1}**	**39.5**	**1.2×10^{3} s^{-1}**	**23.8**
	CA → DehyInt1	8.0×10^{-13} s^{-1}	60.1	3.5×10^{-12} s^{-1}	58.6
	DehyInt1 → DehyInt2	6.9×10^{-8} s^{-1}	48.3	2.0×10^{-10} s^{-1}	54.4
	DehyInt2 → pX + W	1.0×10^{-7} s^{-1}	47.9	4.9×10^{-25} s^{-1}	89.3
	DMF* + E ⇌ CA	$8.1 \times 10^{-6}M^{-1}$ s^{-1}	43.4	3.0×10^{-7} s^{-1}	46.8
2	**CA* → pX + W***	**1.1×10^{7} s^{-1}**	**14.4**	**1.1×10^{-5} M− s^{-1}**	**43.1**
	CA* → DehyInt1*	1.1×10^{7} s^{-1}	14.4	8.9×10^{7} s^{-1}	12.2
	DehyInt1* → DehyInt2*	9.4×10^{7} s^{-1}	12.1	1.5×10^{1} s^{-1}	28.4
	DehyInt2* → pX + W*	3.4×10^{8} s^{-1}	10.8	1.1×10^{-5} M^{-1} s^{-1}	43.1
3	**DMF* + W ⇌ HDI***	**2.7×10^{5} M^{-1} s^{-1}**	**18.2**	**1.3×10^{4} s^{-1}**	**21.3**
No.[a]	**Adsorption/Desorption[b]**	**K_i**	**$\Delta G_{ads,250\ °C}$[d]**		
4	**CA + * ⇌ CA***	**5.84**	**−1.8**		
5	**W + * ⇌ W***	**0.08**	**2.6**		
6	**DMF + * ⇌ DMF***	**35.1**	**−3.7**		
7	**HDI + * ⇌ HDI***	**793**	**−6.9**		
	E + * ⇌ E*	0.05	3.0		
	pX + * ⇌ pX*	0.17	1.9		
	Hept + * ⇌ Hept*	0.003	6.0		

[a]Elementary steps with a number are used to derive the reduced model in which the numbers correspond to the kinetic parameters found in eqs 1−3. Elementary steps without a number are used in the full microkinetic model. [b]Molecules are labeled as follows: DMF = dimethylfuran, E = ethylene, CA = cycloadduct of DMF and ethylene, pX = *p*-xylene, W = water, HDI = 2,5-hexanedione, Hept = Heptane, * = vacant strong acid H−Y site. [c]Subscript "i" implies forward reaction; "−i" implies reverse reaction. [d]Reaction barriers and adsorption energies are tabulated in units of kcal/mol.

the two kinetic regimes. The differences in the apparent activation energies and reaction orders between the two kinetic regimes are predicted by the MKM, with good agreement with experiment. In the linear kinetic regime, the apparent activation

DOI: 10.1021/cs5020783
ACS Catal. 2015, 5, 2367−2375

energies (10.8 kcal/mol from experiment and 18.4 kcal/mol from the MKM) are close to the dehydration reaction barrier of 14.5 kcal/mol calculated from the QM/MM calculations. The ~4 kcal/mol difference between the QM/MM calculation and the microkinetic model is due to contributions from the dehydration and hydrolysis reactions included in the model. The DMF reaction order was 0.49 ± 0.08 from experiment and 0.3 from the microkinetic model. At higher catalyst loadings, the apparent reaction barrier increases (20.1 kcal/mol from experiment and 22.7 kcal/mol from the MKM) and is similar to the Diels–Alder reaction barrier obtained from the QM/MM calculations. In addition, the reaction orders for both DMF and ethylene are close to 1, in support of the homogeneous Diels–Alder reaction mechanism.

The MKM also provides insight into the coverages on the acid sites as a function of conversion (Figure 8B). At early times, the high concentration of DMF in solution causes it to occupy the surface of the zeolite. As DMF is converted and forms *p*-xylene, water, and 2,5-hexanedione, the 2,5-hexanedione that is formed can be seen to almost completely cover the surface of the zeolite. The strong adsorption strength of 2,5-hexanedione allows it to dominate the surface of the zeolite, despite its lower concentrations in solutions relative to DMF and *p*-xylene (Figure 5B). Near complete DMF conversion, however, we see that 2,5-hexanedione is able to reversibly convert back into DMF, driven by the thermodynamics of the system, causing the 2,5-hexanedione to desorb. The strong adsorption strength of the oxanorbornene intermediate allows it to compete with 2,5-hexanedione for active sites, enabling the heterogeneous dehydration pathway. The rapid dehydration of the adsorbed oxanorbornene, however, causes its concentrations on the surface to be very small at all conversions.

3.3. Insights into the Mechanism. From insights obtained from reaction path and model sensitivity analysis, a simplified kinetic model for the reaction of DMF and ethylene to produce *p*-xylene consists of the reactions identified in Table 2. By this simplified reaction mechanism, the rate of *p*-xylene production can be solved as

$$r_{pX} = \frac{k_2 K_1 K_4 [\mathrm{DMF}][\mathrm{E}][\mathrm{H}^+]}{K_6(1 + K_3[\mathrm{W}])[\mathrm{DMF}] + \left(\frac{k_2}{k_{-1}}\right) K_4 [\mathrm{H}^+]} \quad (1)$$

where k_i and K_i are the reaction rate and equilibrium constants for reaction i, [i] is the concentration of component *i*, and $[H^+]$ is the total Brønsted acid active site concentration (for details see the Supporting Information). The functional form of the rate law reveals the presence of two regimes, and its dependence on the concentration of water indicates product inhibition, as water reacts with adsorbed DMF to form 2,5-hexanedione. The reduced model is in good agreement with the microkinetic model; the simplified model is presented as the blue line in Figure 5.

At high Brønsted acid active site concentrations, the $[H^+]$ term in the denominator is dominant and the *p*-xylene production rate reduces to,

$$r_{pX} = k_1[\mathrm{DMF}][\mathrm{E}] \quad (2)$$

The reaction rate depends on the homogeneous Diels–Alder reaction and, therefore, is first-order with respect to DMF and ethylene, in agreement with experiments (Table 1). At sufficiently low Brønsted acid active site concentrations, the first term in the denominator is dominant, and the *p*-xylene production rate instead reduces to

$$r_{pX} = \left(\frac{k_2 K_1 K_4}{K_6(1 + K_3[\mathrm{W}])}\right)[\mathrm{E}][\mathrm{H}^+] \quad (3)$$

The rate has a linear dependence on the Brønsted acid active site concentration, consistent with the findings in the linear regime. In addition, the concentration of DMF appears in both the numerator and the denominator of the rate, and the concentration of ethylene appears only in the numerator. The reduced model supports the variable reaction-order kinetics with respect to DMF (from zero to one) and first-order kinetics with respect to ethylene observed experimentally. The reduced model also supports the experimental trends (Figure 5) and indicates that two regimes is a signature of tandem reactions, specifically of a noncatalyzed reaction followed by a heterogeneously catalyzed second reaction.

5.0. CONCLUSIONS

We have experimentally and computationally studied the kinetics of formation of *p*-xylene by dehydrative aromatization of the Diels–Alder product between 2,5-dimethylfuran and ethylene over H–Y faujasite. This reaction is an archetype of tandem reactions. Cycloaddition proceeds uncatalyzed in solution with a moderate reaction barrier, and dehydration takes place on the active Brønsted acid sites of the zeolite with a low kinetic energy barrier. We have shown that two different kinetic regimes exist dependent upon the reactor loading in H–Y faujasite. At high catalyst loadings, there are enough free active sites to catalyze the dehydration reaction, and as a result, the homogeneous Diels–Alder reaction becomes rate-limiting, consistent with the fact that this is the most energetically demanding step of the mechanism. As the catalyst loading decreases past a critical transition value, the kinetics enters the linear regime where, as a result of an insufficient number of active sites, the dehydrative aromatization becomes rate-limiting, despite the fact that it requires less activation than the cycloaddition reaction.

As we noted in the Introduction, in a study of the same reaction by Wang et al., the rate of formation of *p*-xylene was reported as having a dependence on the density of acid sites. This was explained by an alternative mechanism for the formation of the oxanorbornene derivative that did not involve Diels–Alder cycloaddition.[20] This finding was at odds with the kinetic studies of Williams et al., who reported that the rate of *p*-xylene production over H–Y was independent of the density of active sites.[19] We believe that the two kinetic regimes reported and analyzed here can reconcile these two seemingly opposing views. In Williams et al., the reaction was carried out at 300 °C, with an effective catalyst loading range of 1.7–3.2 mM, which is in the flat, cycloaddition-limited regime and, thus, independent of catalyst loading. On the other hand, in Wang et al., the experiments were performed at 250 °C and significantly lower loadings, ~0.2 mM of effective acid site concentration, which lies in the dehydration-limited regime and which explains the reported dependence of the rate on the density of active sites.

Although available acid sites and site acidity may influence the rate of change of the rate of the reaction with acid concentration in the dehydration regime (the slope of the curve in Figure 5A), the plateau should remain unaffected because it is determined by the uncatalyzed cycloaddition reaction rate.

DOI: 10.1021/cs5020783
ACS Catal. 2015, 5, 2367–2375

Thus, the cycloaddition-limited regime should be "universal" to all (Brønsted acid) catalysts. Given that the maximum rate is controlled by the cycloaddition reaction, a logical next step to optimize the process is to develop methods to accelerate the Diels–Alder reaction.

■ ASSOCIATED CONTENT

Supporting Information

The following file is available free of charge on the ACS Publications website at DOI: 10.1021/cs5020783.

Investigation of gas-to-liquid mass transfer limitations, reaction network and energetics considered in the microkinetic model, development of rate expressions, design of experiment (DOE) to access model uncertainty, reduced model development, catalyst preparation and characterization, and additional references (PDF)

■ AUTHOR INFORMATION

Corresponding Authors

*E-mail: cstavros@udel.edu.
*E-mail: hauer@umn.edu.
*E-mail: vlachos@udel.edu.

Notes

The authors declare no competing financial interest.
⊥R.E.P., N.N., and C.L.W. contributed equally.

■ ACKNOWLEDGMENTS

We acknowledge support from the Catalysis Center for Energy Innovation, an Energy Frontier Research Center funded by the U.S. Department of Energy, Office of Science, Office of Basic Energy Sciences under Award No. DE-SC0001004. This research used resources of the National Energy Research Scientific Computing Center, a DOE Office of Science User Facility supported by the Office of Science of the U.S. Department of Energy under Contract No. DE-AC02-05CH11231.

■ REFERENCES

(1) Vlachos, D. G.; Chen, J. G.; Gorte, R. J.; Huber, G. W.; Tsapatsis, M. *Catal. Lett.* **2010**, *140*, 77–84.
(2) Binder, J. B.; Raines, R. T. *J. Am. Chem. Soc.* **2009**, *131*, 1979–1985.
(3) Bruijnincx, P. C. A.; Weckhuysen, B. M. *Angew. Chem., Int. Ed.* **2013**, *52*, 11980–11987.
(4) Dauenhauer, P. J.; Huber, G. W. *Green Chem.* **2014**, *16*, 382–383.
(5) Ragauskas, A. J.; Williams, C. K.; Davison, B. H.; Britovsek, G.; Cairney, J.; Eckert, C. A.; Frederick, W. J., Jr.; Hallett, J. P.; Leak, D. J.; Liotta, C. L.; Mielenz, J. R.; Murphy, R.; Templer, R.; Tschaplinski, T. *Science* **2006**, *311*, 484–489.
(6) Kwart, H.; Burchuk, I. *J. Am. Chem. Soc.* **1952**, *74*, 3094–3097.
(7) Wenkert, E.; Moeller, P. D. R.; Piettre, S. R. *J. Am. Chem. Soc.* **1988**, *110*, 7188–7194.
(8) Chen, C.-H.; Rao, P. D.; Liao, C.-C. *J. Am. Chem. Soc.* **1998**, *120*, 13254–13255.
(9) Román-Leshkov, Y.; Barrett, C. J.; Liu, Z. Y.; Dumesic, J. A. *Nature* **2007**, *447*, 982–986.
(10) Chidambaram, M.; Bell, A. T. *Green Chem.* **2010**, *12*, 1253–1262.
(11) van Haveren, J.; Scott, E. L.; Sanders, J. *Biofuels, Bioprod. Biorefin.* **2008**, *2*, 41–57.
(12) Phillips, C. B.; Datta, R. *Ind. Eng. Chem. Res.* **1997**, *36*, 4466–4475.
(13) Nikbin, N.; Do, P. T.; Caratzoulas, S.; Lobo, R. F.; Dauenhauer, P. J.; Vlachos, D. G. *J. Catal.* **2013**, *297*, 35–43.
(14) Nikbin, N.; Feng, S.; Caratzoulas, S.; Vlachos, D. G. *J. Phys. Chem. C* **2014**, *118*, 24415–24424.
(15) Tomás, R. A. F.; Bordado, J. C. M.; Gomes, J. F. P. *Chem. Rev.* **2013**, *113*, 7421–7469.
(16) Pacheco, J. J.; Davis, M. E. *Proc. Natl. Acad. Sci. U.S.A.* **2014**, *111*, 8363–8367.
(17) Chang, C.-C.; Green, S. K.; Williams, C. L.; Dauenhauer, P. J.; Fan, W. *Green Chem.* **2014**, *16*, 585–588.
(18) Do, P. T. M.; McAtee, J. R.; Watson, D. A.; Lobo, R. F. *ACS Catal.* **2013**, *3*, 41–46.
(19) Williams, C. L.; Chang, C.-C.; Do, P.; Nikbin, N.; Caratzoulas, S.; Vlachos, D. G.; Lobo, R. F.; Fan, W.; Dauenhauer, P. J. *ACS Catal.* **2012**, *2*, 935–939.
(20) Wang, D.; Osmundsen, C. M.; Taarning, E.; Dumesic, J. A. *ChemCatChem* **2013**, *5*, 2044–2050.
(21) Li, Y.-P.; Head-Gordon, M.; Bell, A. T. *J. Phys. Chem. C* **2014**, *118*, 22090–22095.
(22) Woodward, R. B.; Hoffmann, R. *Angew. Chem., Int. Ed.* **1969**, *8*, 781–853.
(23) Zhuze, T. P.; Zhurba, A. S. *Bull. Acad. Sci. USSR, Div. Chem. Sci. (Engl. Transl.)* **1960**, *9*, 335–337.
(24) Marenich, A. V.; Cramer, C. J.; Truhlar, D. G. *J. Phys. Chem. B* **2009**, *113*, 6378–6396.
(25) Zhao, Y.; Truhlar, D. G. *Theor. Chem. Acc.* **20072008**, *120*, 215–241.
(26) Baerlocher, C.; McCusker, L. B. *Database of Zeolite Structures.* http://www.iza-structure.org/databases (accessed Feb 11, 2015).
(27) Svensson, M.; Humbel, S.; Froese, R. D. J.; Matsubara, T.; Sieber, S.; Morokuma, K. *J. Phys. Chem.* **1996**, *100*, 19357–19363.
(28) Dapprich, S.; Komáromi, I.; Byun, K. S.; Morokuma, K.; Frisch, M. J. *J. Mol. Struct.: THEOCHEM* **1999**, *461*, 1–21.
(29) Vreven, T.; Morokuma, K.; Farkas, Ö.; Schlegel, H. B.; Frisch, M. J. *J. Comput. Chem.* **2003**, *24*, 760–769.
(30) Rappé, A. K.; Casewit, C. J.; Colwell, K. S.; Goddard, W. A.; Skiff, W. M. *J. Am. Chem. Soc.* **1992**, *114*, 10024–10035.
(31) Frisch, M. J.; Trucks, G. W.; Schlegel, H. B.; Scuseria, G. E.; Robb, M. A.; Cheeseman, J. R.; Scalmani, G.; Barone, V.; Mennucci, B.; Petersson, G. A.; Nakatsuji, H.; Caricato, M.; Li, X.; Hratchian, H. P.; Izmaylov, A. F.; Bloino, J.; Zheng, G.; Sonnenberg, J. L.; Hada, M.; Ehara, M.; Toyota, K.; Fukuda, R.; Hasegawa, J.; Ishida, M.; Nakajima, T.; Honda, Y.; Kitao, O.; Nakai, H.; Vreven, T.; Montgomery, J. A., Jr.; Peralta, J. E.; Ogliaro, F.; Bearpark, M.; Heyd, J. J.; Brothers, E.; Kudin, K. N.; Staroverov, V. N.; Kobayashi, R.; Normand, J.; Raghavachari, K.; Rendell, A.; Burant, J. C.; Iyengar, S. S.; Tomasi, J.; Cossi, M.; Rega, N.; Millam, J. M.; Klene, M.; Knox, J. E.; Cross, J. B.; Bakken, V.; Adamo, C.; Jaramillo, J.; Gomperts, R.; Stratmann, R. E.; Yazyev, O.; Austin, A. J.; Cammi, R.; Pomelli, C.; Ochterski, J. W.; Martin, R. L.; Morokuma, K.; Zakrzewski, V. G.; Voth, G. A.; Salvador, P.; Dannenberg, J. J.; Dapprich, S.; Daniels, A. D.; Farkas, Ö.; Foresman, J. B.; Ortiz, J. V.; Cioslowski, J.; Fox, D. J. *Gaussian 09 (Rev. A.2)*; Gaussian Inc.: Wallingford, CT, 2009.
(32) Nikbin, N.; Caratzoulas, S.; Vlachos, D. G. *ChemSusChem* **2013**, *6*, 2066–2068.

DOI: 10.1021/cs5020783
ACS Catal. 2015, 5, 2367–2375